AIAA JOURNAL
Vol. 55, No. 7, July 2017

Nonlinear Thermal Reduced-Order Modeling for Hypersonic Vehicles

Ryan J. Klock* and Carlos E. S. Cesnik†
University of Michigan, Ann Arbor, Michigan 48109

DOI: 10.2514/1.J055499

A set of reduced-order models are considered to determine the variation of the material thermal capacity and thermal conductivity with respect to temperature for a representative hypersonic vehicle structure on a terminal trajectory. The number of thermal degrees of freedom is first reduced by projecting the thermal state of a sample structure into a modal space whose bases are determined using proper orthogonal decomposition. A numerical integration scheme based on the Crank–Nicolson algorithm is used to simulate the thermal state forward in time. Models for the generalized material thermal properties are based on the method of kriging, a least-squares polynomial approximation, and a singular value decomposition approach. The resulting thermal models are compared in terms of accuracy and computational efficiency. The singular value decomposition approach is shown to be the superior overall reduced-order model to capture the variation of thermal properties with temperature when compared to a full-order finite element solution. The effects of varying the number of retained thermal modes and thermal property eigenvectors on the singular value decomposition model are then considered. It is shown that only a few eigenvectors need to be considered to achieve excellent agreement with finite element analysis.

Nomenclature

A	=	thermal snapshot matrix
B	=	single snapshot vector of vectorized generalized heat capacity and thermal conductivity matrices
$\bar{B}$	=	snapshot matrix of vectorized generalized heat capacity and thermal conductivity matrices as columns
$\tilde{B}$	=	approximate snapshot of vectorized generalized heat capacity and thermal conductivity matrices
c	=	thermal basis coefficients vector
c_i	=	ith entry of a thermal basis coefficients vector
$\bar{c}$	=	complete polynomials thermal basis coefficients matrix
$\tilde{c}$	=	unsampled thermal basis coefficients vector
F	=	finite element thermal load vector, W
f	=	generalized thermal load vector
K	=	finite element thermal conductivity matrix, W/K
k	=	generalized thermal conductivity matrix
$k_{i,j}$	=	entry of the ith row and jth column of a generalized thermal conductivity matrix
L_∞	=	maximum error
M	=	finite element heat capacity matrix, J/K
M_e	=	Mach number external to a flow boundary layer
m	=	generalized heat capacity matrix
$m_{i,j}$	=	entry of the ith row and jth column of a generalized heat capacity matrix
n	=	number of training samples
o	=	number of testing samples
p_e	=	static pressure external to a flow boundary layer, Pa
$\dot{q}_w$	=	wall heat flux in, W/m^2
R_{ls}	=	least-squares fit coefficient matrix
R_{svd}	=	right singular vectors correlation matrix
r	=	number of thermal bases
T	=	temperature vector, K
T_e	=	static temperature external to a flow boundary layer, K
T_w	=	wall temperature, K
t	=	time, s
t_n	=	discrete time at level n, s
U	=	left singular vectors matrix
V	=	right singular vectors matrix
x	=	spatial coordinate along the x direction, m
y	=	spatial coordinate along the y direction, m
z	=	spatial coordinate along the z direction, m
Δt	=	discrete time interval, s
ϵ_{rel}	=	relative energy loss of thermal basis projection
Σ	=	diagonal singular values matrix
ψ	=	thermal basis matrix
$\|\|$	=	matrix norm

Received 11 July 2016; revision received 5 January 2017; accepted for publication 23 January 2017; published online 24 April 2017.

*Ph.D. Candidate, Department of Aerospace Engineering. Student Member AIAA.

†Professor, Department of Aerospace Engineering. Fellow AIAA.

I. Introduction

HIGH-SPEED flight systems, particularly hypersonic vehicles, operate in a high-energy environment characterized by strong fluid, thermal, and structural interactions. Because of a lack of ground-test facilities that can generate the high-energy environment of interest, the primary focus for hypersonic vehicle design and preliminary evaluation must be through analytical and computational simulations. Current computational research efforts have focused on either improving particular physics model fidelity with limited discipline interactions due to a high computational cost or including many discipline interactions using very simple models. Thus, there is a wide middle ground between the low-fidelity, high-interaction and high-fidelity, low-interaction modeling regimes that has yet to be considered but is critical to the development of high-speed flight systems.

In this work, a scramjet-propelled hypersonic vehicle is considered. Such a vehicle is typically flown at conditions of high dynamic pressure, leading to trajectories of relatively low altitudes and high speeds for an airbreathing vehicle. Under such flight conditions, aerodynamic heating becomes a driving factor in the design as high surface temperatures and heat flux seep into the structure and modify the elastic characteristics of the vehicle. Critical to accurate determination the thermal state of the structure is consideration of the variation of the material thermal properties with temperature, specifically thermal conductivity and heat capacity.

Past works [1–4] have demonstrated that reduction of the thermal problem is possible by identification of appropriate basis modes and projection of the governing equations into the space spanned by these modes. Modal identification using proper orthogonal decomposition (POD) [5,6], typically through the method of snapshots, has been used to derive orthogonal thermal basis modes that could then be linearly combined to approximate the temperature distribution of a

structure. However, the variation of the thermal conductivity and heat capacity of the materials was not considered.

The variation of material thermal properties has been considered in other literature, although often in a limited capacity. In a study by McMasters et al. [7] of nonlinear thermal diffusion, an exact analytical solution was derived with a thermal conductivity that varied linearly with temperature and was later used to verify the results of a finite element thermal analysis code, CALORE. Although thermal conductivity was variable, all other thermal properties were assumed to be constant.

Matney et al. [8] considered the variation of thermal properties for the problem of hypersonic flow over a panel with underlying stiffeners in the development of an adaptive thermal basis set. In their study, aerodynamic pressure was modeled using piston theory [9], and heat flux was modeled using the Eckert reference enthalpy method [10]. These aerodynamic and thermal loading solutions where then applied to a finite element model (FEM) to observe structural and thermal responses. Variation of the in-plane thermal conductivity with respect to the temperature of the panel was modeled using a property lookup table. Each element of their panel FEM was identical and could use the same lookup table for all elements. This approach to modeling the variation of material thermal properties with respect to temperature was therefore limited to very simple geometries where uniform finite elements could be used.

The force-derivative method originally developed by Camarda et al. [11,12] for nonlinear structural dynamics has also been shown by Balakrishnan et al. [13] to work well for nonlinear thermal problems by modifying the heat load based on previously linearized thermal capacity and conductivity properties. In this approach, variation of the thermal properties of both structures and materials could be considered but required repeatedly solving an eigenproblem and inverting a variable FEM conductivity matrix. This allows for transient thermal solutions more quickly than a full FEM simulation but not without its own overhead, which could become prohibitive if more than a couple degrees of freedom are considered.

For the study presented in this paper, a representative substructure of the hypersonic vehicle developed by Pasiliao et al. [14] using the Preliminary Aerothermal Structural Simulation code suite is considered. This vehicle is an air-launched, rocket–scramjet combined cycle propelled vehicle, which performs a three-phase trajectory. Shown in Fig. 1, the vehicle would first boost under rocket propulsion up to a cruising altitude above 50 kft (15.2 km) and airspeed above Mach 5. The rocket booster would then be jettisoned and a scramjet engaged to maintain a mostly steady and level cruise condition. Finally, after exhausting the scramjet fuel supply, the vehicle would enter an unpropelled terminal phase to reach a ground target some distance downrange.

Witeof and Neergaard [15] performed material trade and sizing optimization studies of thermal protection systems (TPSs) and structural elements to minimize mass while satisfying material temperature and stiffness constraints. In their trade study, aerodynamic heating was approximated using the Aerothermal Target Analysis Program [16]. Structural modes were approximated using Timoshenko beam elements, and the variation in modal frequencies due to thermal effects was investigated with respect to flight time.

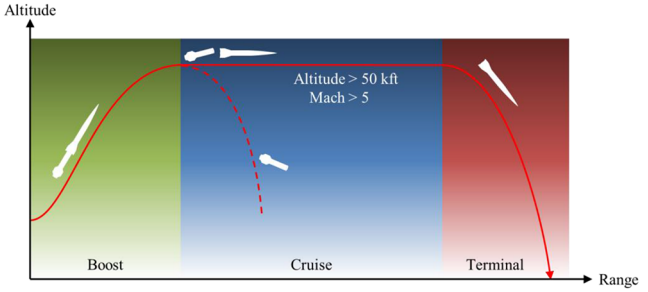

Fig. 1 Basic outline of a boost–cruise–terminal mission profile for an air-launched, rocket-boosted hypersonic vehicle.

The thermal state of the vehicle in the terminal phase is the main focus of this paper. In this phase, the highest structural temperatures are experienced and are most likely to impact the flight characteristics of the vehicle. It is also in this phase that an accurate model of the vehicle state is required to maximize strike accuracy and effectiveness. To first reduce the order of the thermal problem, the method of POD is applied and the governing equations generalized with the resulting basis set. Then, to capture the influence of structural temperature on thermal conductance and capacitance, three reduced-order models (ROMs) are investigated: least-squares fit multidimensional polynomials, the method of kriging, and a newly developed method based on a combination of singular value decomposition [17] and linear correlation.

II. Theoretical Development

A. Proper Orthogonal Decomposition

A common method to reduce the dimensionality of the thermal problem is to apply proper orthogonal decomposition (POD). POD is a statistical method in which empirical data are used to identify correlated features, or modes, of a system and is optimal in the sense that the fewest number of modes may be used to represent the majority of the system energy. The retention of only the most dominant modes allows for the creation of a basis that captures the overall behavior of the system while significantly reducing the number of degrees of freedom. The ultimate goal is then to represent the thermal state of a system as a sum of basis modes and time-varying coefficients, i.e.,

$$T(t) = \Psi c(t) \tag{1}$$

where $T(t)$ is a column vector of time-varying temperatures at predefined locations of interest, such as finite element nodes, centroids, or integration points; Ψ is the thermal basis matrix whose columns are the thermal basis modes; $c(t)$ is a column vector of the time-varying coefficients for each basis mode; and t is time. The basis matrix Ψ is determined by consideration of a snapshot matrix A whose columns are vectors of temperatures at specific moments during a high-fidelity heat-transfer simulation, such as a finite element analysis (FEA) solution. The error incurred by representing the thermal state with a truncated thermal basis matrix may be interpreted as the relative energy lost (ε_{rel}) by projecting the snapshot matrix A onto the space spanned by the truncated thermal basis matrix Ψ, given by [1]

$$\varepsilon_{\text{rel}} = \frac{\|A - \Psi\Psi^T A\|^2}{\|A\|^2} \tag{2}$$

For brevity, a full description of the POD method is omitted; however, a thorough description of this method's application to thermal problems is given in [1].

B. Generalization of Thermal Problem

Once an appropriate thermal basis is determined, one may generalize the governing system of equations for the thermal problem

$$M(T(t))\dot{T}(t) + K(T(t))T(t) = F(t) \tag{3}$$

into

$$m(c(t))\dot{c}(t) + k(c(t))c(t) = f(t) \tag{4}$$

where

$$m(c(t)) = \Psi^T M(\Psi c(t))\Psi \tag{5a}$$

$$k(c(t)) = \Psi^T K(\Psi c(t))\Psi \tag{5b}$$

$$f(t) = \Psi^T F(t) \tag{5c}$$

and where $M(T)$ and $K(T)$ are the thermal capacity and conductivity matrices, each a function of the time-varying temperature vector $T(t)$, and $F(t)$ is the time-varying thermal load vector.

C. Numerical Integration

To numerically integrate the generalized thermal problem forward at discrete times t_n and t_{n+1}, separated by the time interval Δt, the Crank–Nicolson algorithm is considered due to its known unconditional stability for both linear and nonlinear heat conduction systems [18]. This results in

$$c(t_{n+1}) = \left[\frac{k}{2} + \frac{m}{\Delta t}\right]^{-1} \left\{ \left[-\frac{k}{2} + \frac{m}{\Delta t} \right] c(t_n) + \frac{f(t_n) + f(t_{n+1})}{2} \right\} \quad (6)$$

D. Modeling Generalized Temperature-Dependent Material Thermal Properties

1. Least-Squares Fit Polynomials

The first method considered is to approximate each entry of the generalized thermal matrices using polynomials formed from the thermal mode coordinates, i.e.,

$$B \approx R_{\text{ls}}[1 \ \cdots \ 1 \ c_1 \ \cdots \ c_r \ c_1c_1 \ c_1c_2 \ \cdots \ c_rc_r \ c_1c_1c_1 \ c_1c_1c_2 \ \cdots]^T = R_{\text{ls}}\bar{c} \quad (7)$$

where R_{ls} is a matrix of coefficients for each permutation of thermal mode coordinates c_i, where i varies from 1 to r for each thermal basis, and B contains the entries of the thermal matrices k and m stored as column vectors:

$$B = [k_{1,1} \quad k_{1,2} \quad \cdots \quad k_{r,r} \quad m_{1,1} \quad m_{1,2} \quad \cdots \quad m_{r,r}]^T \quad (8)$$

The coefficient matrix R_{ls} is determined by the solution to the least-squares problem:

$$R_{\text{ls}} = (\bar{c}\bar{c}^T)^{-1}\bar{c}\,\bar{B} \quad (9)$$

where $\bar{c}$ is a matrix whose columns are vectors of the thermal mode coordinates for each snapshot expanded to include all powers and combinations of the modal coordinates desired for the polynomial to be fit; and $\bar{B}$ is a matrix whose columns are vectors of the entries of the thermal matrices k and m corresponding to each set of thermal coordinates.

2. Kriging

The second method considered to capture the variation of the thermal capacity and conductivity matrices with respect to the thermal modal coordinates, $m(c)$ and $k(c)$, is kriging [19]. Kriging is a statistics-based method that can incorporate the trend model properties of a more typical linear or polynomial regression with the spatial correlation properties of kernel-based approximation methods [20]. It provides flexible and computationally efficient models that may be adapted to represent many complex n-dimensional response surfaces. Kriging is a useful approximation of computer analysis in particular, where no random error is present, due to the method's ability to exactly recover the solutions of the training points used to create it.

To create the kriging model, a set of training samples of thermal conductivity and capacity matrices is produced from a heat-transfer FEM based on coordinates of the thermal modal basis. Selection of the modal coordinates is determined by Latin hypercube sampling (LHS) [21,22] within thermal coordinate bounds determined by the extremes observed in the POD snapshot matrix previously described. Upon collection of a number of model training and testing samples, several kriging models may be constructed based on different combinations regression and correlation functions, many of which are available in the Matlab DACE Toolbox [23]. Each model is then tested for accuracy in reproducing the test samples by a root-mean-squared-error (RMSE) and maximum normalized error (norm L_∞).

3. Singular Value Decomposition

The third method is a new approach that uses singular value decomposition (SVD) and nonlinear correlation. This method is modeled after [24], which used a similar approach to efficiently approximate the aerodynamic loads of a maneuvering aircraft. For the application of determining the entries of the generalized thermal capacity and conductivity matrices, a sampling of the FEM solutions is first required. These are taken using the same LHS as the kriging ROM generation for direct comparison of the methods. A snapshot matrix $\bar{B}$ is constructed with the entries of $k(c)$ and $m(c)$ as column vectors at each LHS point and may be represented as

$$U\Sigma V^T = \bar{B} \quad (10)$$

where U is a square matrix whose columns are the left singular vectors of $\bar{B}$, Σ is a rectangular diagonal matrix of the singular values, and V is a square matrix whose columns are the right singular vectors of $\bar{B}$. Because of the arrangement of the snapshot matrix $\bar{B}$, U may be thought of as a set of orthogonal unit vectors that span the space populated by the snapshots, Σ as the relative importance of each unit vector to describing that space, and V as a list of coefficients corresponding to the location of each snapshot in the space.

If the space spanned by the columns of $\bar{B}$ is large (i.e., each snapshot contains a large number of degrees of freedom), the problem may be reduced by removing the smallest singular values in Σ as well as the corresponding columns of U and V. In this way, dimensions of the snapshots that are least important to the representation of $\bar{B}$ may be ignored, and the order of the eventual model is reduced.

The next step is to relate the coordinates of each snapshot stored in V to the thermal coordinate inputs $\bar{c}$. A correlation matrix R_{svd} is determined that relates the basis amplitudes in V to the thermal mode coordinates for each snapshot stored as column vectors in matrix $\bar{c}$ using a least-squares fit:

$$\bar{c}^T R_{\text{svd}} = V \quad (11)$$

$$R_{\text{svd}} = (\bar{c}\bar{c}^T)^{-1}\bar{c}V \quad (12)$$

Then, given any additional set of thermal mode coordinates $\tilde{c}$, not necessarily included in the snapshot matrix, an estimated snapshot matrix $\tilde{B}$ may be found by

$$\tilde{B} = U\Sigma R_{\text{svd}}^T \tilde{c} \quad (13)$$

such that the columns of $\tilde{B}$ contain approximate entries of the thermal matrices k and m. Thus, $k(c)$ and $m(c)$ are readily available during integration of the thermal problem.

III. Test Case Example

A. Structural Model

To compare each ROM approach, a sample FEM was established that was representative of a small portion of the hypersonic vehicle proposed by Pasiliao et al. [14] and later refined by Witeof and Neergaard [15]. This substructure was located at the interface of the vehicle nose ballast and forebody, on the Earth-facing side during typical flight conditions, in a region that was previously shown in [25] to experience high thermal loads and contain several different materials. For simplicity, this substructure was considered to be approximately two-dimensional, despite the curvature of the vehicle's body in this region. The vehicle, sample substructure, and FEM grid are shown in Fig. 2. The FEM consisted of 6478 nodes and 3040 linear hexahedral solid elements clustered near regions where high-temperature gradients were expected due to external heat flux or material interfaces. Three materials are considered: elemental tungsten in the nose ballast, Exelis Inc.'s Acusil-II material in the thermal protection layer covering the forebody, and titanium alloy Ti-6Al-4V, which comprised the structural monocoque of the vehicle. For simplicity, neighboring materials were considered to be perfectly bonded, and no joiner or fastener geometry was included. Boundaries of the FEM that were not exposed to the external heat flux were adiabatic.

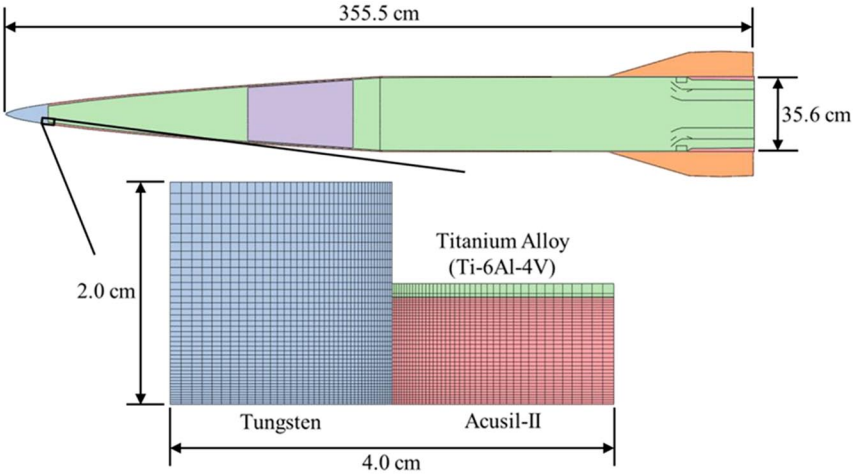

Fig. 2 Sample substructure with overlaid FEM grid and its location on the vehicle.

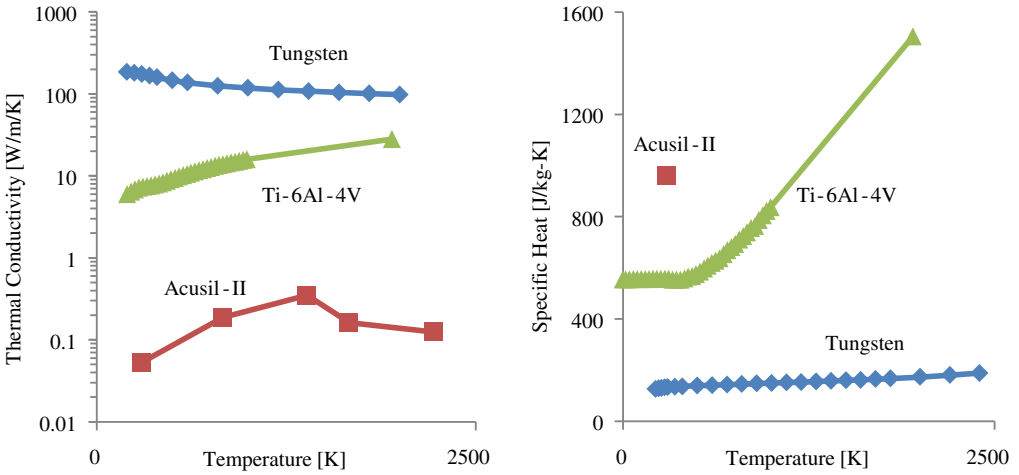

Fig. 3 Large variation of thermal properties due to temperature [26–33].

B. Material Thermal Properties

Experimental thermal properties of the materials considered in the FEM are given in Fig. 3 [26–33]. Only one data point was available for the specific heat capacity of the Acusil-II material due to its proprietary nature. However, with all other thermal properties over the temperature range of interest, the substructure and material set presented a highly nonlinear system on which to compare the thermal ROM approaches.

C. Sample Collection

To create the thermal property ROMs, a number of training and testing samples were required. The process used to collect these samples is outlined in Fig. 4 and begins with considering the thermal bases Ψ and thermal mode ranges $\min(c)$ and $\max(c)$ resulting from a POD of an FEA heat transfer simulation of the substructure. Latin hypercube sampling was used to determine a uniformly random set of thermal coordinates c, which were then converted to physical temperature distributions T within the FEM. These were then passed to an FEA solver, which assembled the full thermal property matrices M and K, which were then exported and generalized according to the thermal bases Ψ into m and k. Each generalized thermal property matrix was then paired with its corresponding thermal coordinates c and sent to each of three ROM training functions to be incorporated into a thermal property ROM.

Within each ROM training function, the c, m, and k samples are divided into two groups. One group of n training samples was used to train each model within the ROM type. For the least-squares ROM, three models were considered: linear, quadratic, and cubic polynomials of the thermal coordinates c. The kriging ROM contained 18 combinations of three regression functions (constant, linear, and quadratic polynomials) and six correlation functions (pure exponential, general exponential, Gaussian, linear, spherical, and spline). Each of these regression and correlation functions were default forms provided with the Matlab DACE toolbox [23]. The SVD and linear correlation ROM contained three models: linear, quadratic, and cubic polynomials of the thermal coordinates.

Another group of o testing samples was then used to test the accuracy of each model in prediction of samples not contained in the training set. The model that contained the least single entry maximum error (L_∞) normalized by the value each entry was considered the most accurate and exported for comparison against the other ROM types. The L_∞ error metric was selected to compare the different ROM variants within a training function because it is the most conservative measure of error. A flowchart of this process is shown in Fig. 5.

IV. Results and Discussion

A. Finite Element Analysis Heat Transfer Simulation

To determine a suitable POD basis set for the substructure, a high-fidelity heat transfer simulation was performed using the Dassault Systèmes Inc.'s Abaqus FEA [34] heat transfer solver. During simulation, at every time step, the wall temperature T_w, time t, and spatial locations x, y, z of every node exposed to flow were exported to a Fortran user-defined subroutine and used to search for a corresponding node in a preprocessed database of flow conditions, namely pressure p_e, temperature T_e, and Mach number M_e. This database was determined a priori by an in-house unsteady aerodynamics code employing oblique shock, Prandtl–Meyer

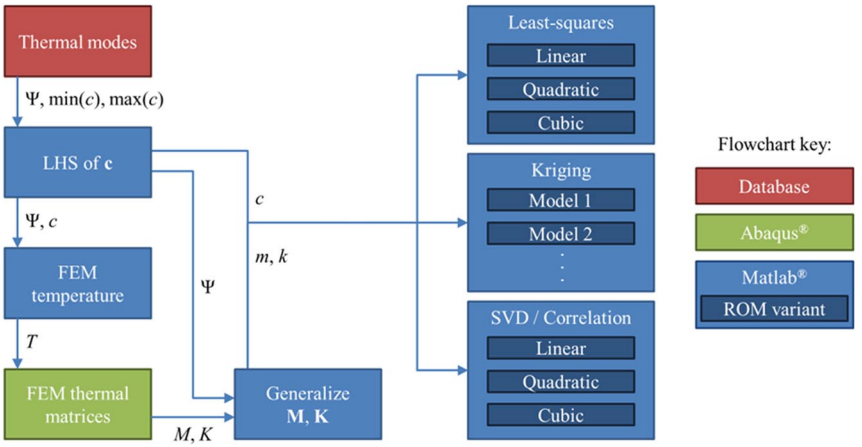

Fig. 4 Training sample collection process.

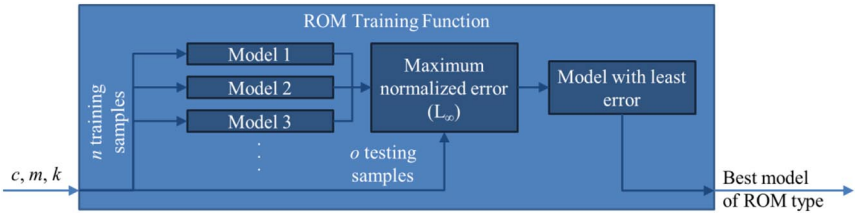

Fig. 5 ROM training, testing, and selection for each ROM type.

expansion, and third-order piston theory [9]. The flight trajectory consisted of a 520 s, Mach 6, 75 kft (22.9 km) altitude cruise phase, during which the vehicle was trimmed for propelled steady and level flight, followed by a 37.5 s unpropelled terminal phase along a path optimized for maximum final kinetic energy. Details of this trajectory and optimization process may be found in [25]. Once the flow properties near a node of interest were found, the Eckert reference temperature [10] and black-body radiation methods were used to determine the heat flux $\dot{q}_w$ to the node. The heat flux was imported back to the FEA heat transfer solver as a boundary condition, and the solution was moved ahead in time. A flowchart of this process is shown in Fig. 6. The resulting temperature profiles of the substructure during the cruise and terminal phases are shown in Figs. 7 and 8, respectively.

During the cruise phase, the substructure is initially a uniform 238 K. The outer surface of the TPS quickly warms to nearly 1277 K and begins slowly conducting heat inward toward the skin. The ballast meanwhile has a high thermal conductivity and warms almost uniformly. Protected by the TPS, the skin is the slowest to warm; however, after roughly 320 s, the substructure became completely thermally soaked, meaning nearly a uniform 1277 K. Upon entering the terminal phase, the vehicle switched from a nose-up to a nose-down angle of attack. Thus, the substructure, which was initially on the highly thermal loaded windward side of the vehicle, was then on the less-loaded leeward side, which caused a small initial drop in the outer TPS temperature. After about 32 s, the vehicle had sufficiently slowed to allow additional cooling of the TPS until the end of the terminal phase at 37.5 s. Throughout the terminal phase the skin remained nearly at 1277 K because insufficient time passed to conduct its heat back out through the TPS.

B. Thermal Bases

After performing a simulation of the sample structure along the cruise and terminal phase trajectories, thermal bases were determined using the method of POD for the terminal phase. The first five bases are shown in Fig. 9, with the relative eigenvalue magnitudes and basis truncation error shown in Fig. 10. Figure 9 reveals that almost the entirety of all modes focus on describing the temperature gradient in the TPS of the model due to the low conductivity of the Acusil-II material compared to the tungsten and titanium alloy of the ballast

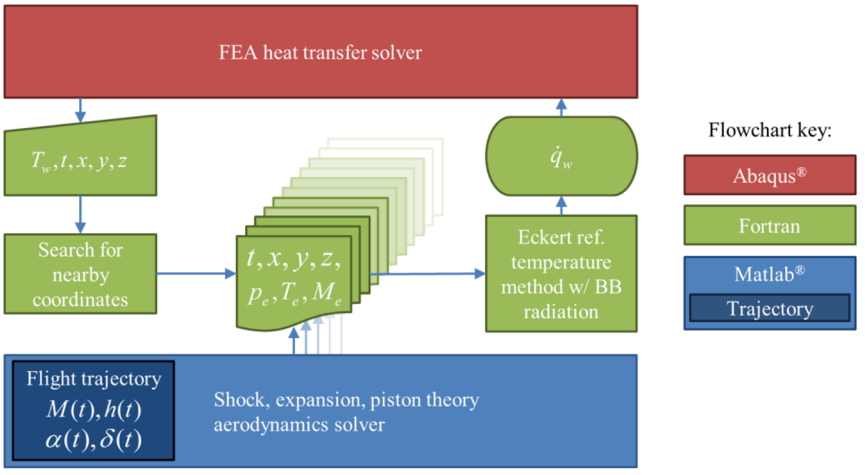

Fig. 6 FEA heat transfer simulation along flight trajectory.

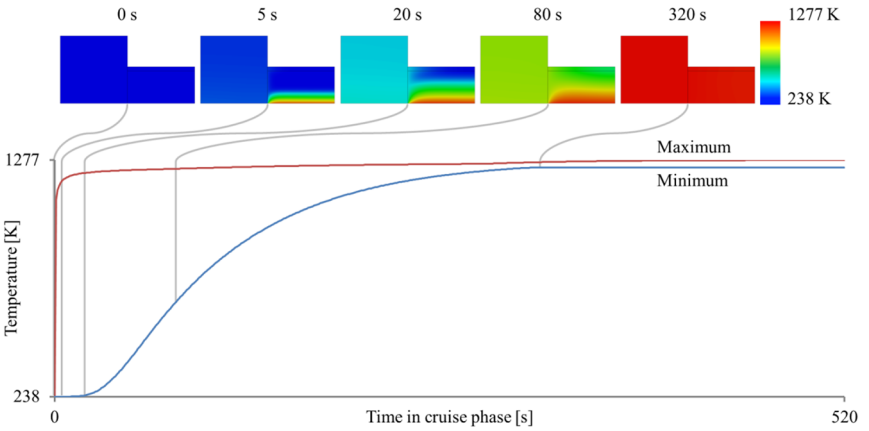

Fig. 7 Temperature range in substructure during cruise phase.

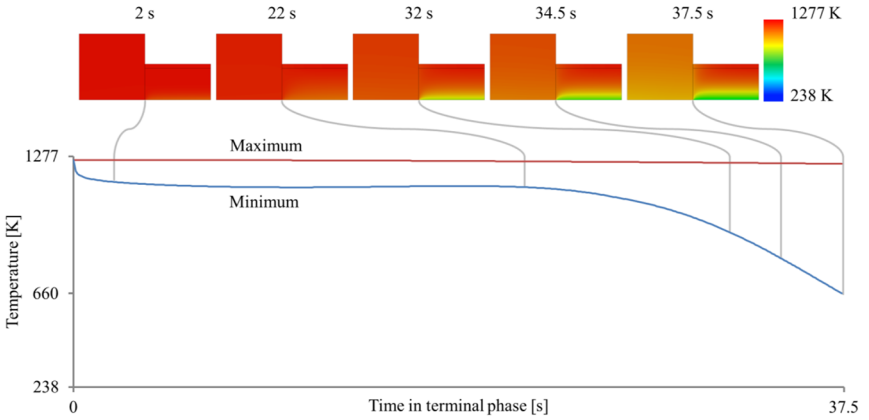

Fig. 8 Temperature range in substructure during terminal phase.

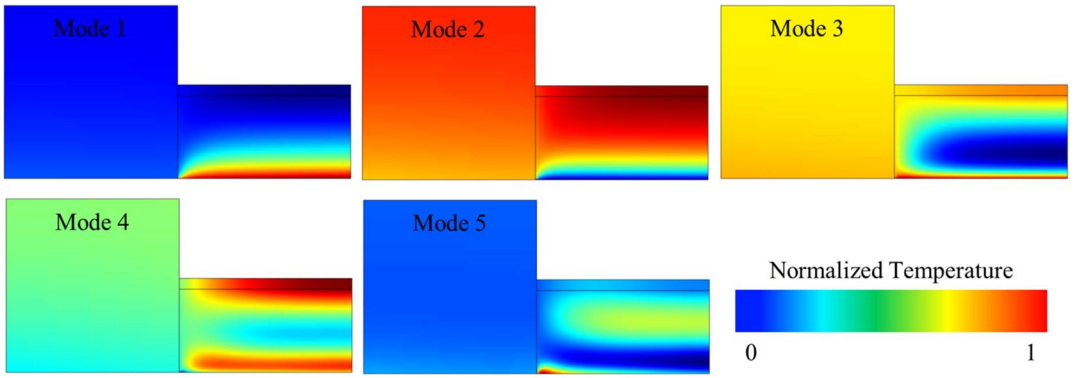

Fig. 9 First five most prominent POD thermal modes.

and skin, respectively. Some detail is afforded for the titanium alloy skin; however, this is largely to enforce the temperature continuity between the skin and TPS. Despite placing almost all focus on the TPS, Fig. 10 shows that the truncation of the bases to the first five modes provided a relative error of $\sim 10^{-8}$, which is typically sufficient to accurately represent the thermal state of the structure. Thus, one may use these bases to generalize the rank 6478 thermal problem considered by the FEA to a rank 5 problem and be confident that reasonable solution accuracy may still be obtained if similar thermal loading is simulated.

C. Reduced-Order Model Accuracy

For each ROM type, the number n of training samples was varied by powers of 2 from $n = 2$ to 1024. Each of the resulting models was then testing using the same $k = 1000$ samples to evaluate each ROM's accuracy. The root-mean-squared error (RMSE) and normalized maximum error (norm L_∞) of each ROM type are shown in Fig. 11, with the most accurate of each type compared in Fig. 12. For all ROM types, the higher-order regression and polynomial functions resulted in the lowest errors when a sufficient number of training samples were provided. However, if too few training samples were provided, the higher orders often resulted in higher errors than their lower-order counterparts, especially for the least-squares and SVD models. For $n > 200$, both the least-squares and SVD ROMs did not exhibit a reduction in error given further training samples. This was due to the limitation of their maximum cubic polynomial function order. The kriging method produced two distinct groups of models. The first was when the zeroth-order polynomial regression was used. This allowed kriging models to be constructed using very few training samples and is akin to radial basis function type ROMs. However, once $n \geq 8$, first and then second-order regression polynomials were shown to be superior. For all kriging ROMs, the

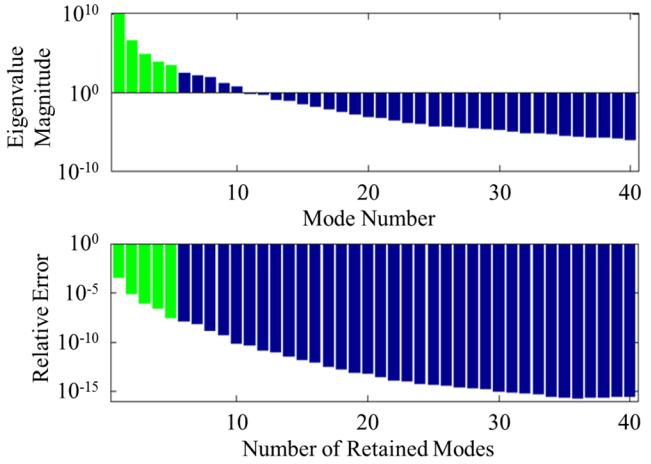

Fig. 10 Relative POD eigenvalue magnitude and truncation error.

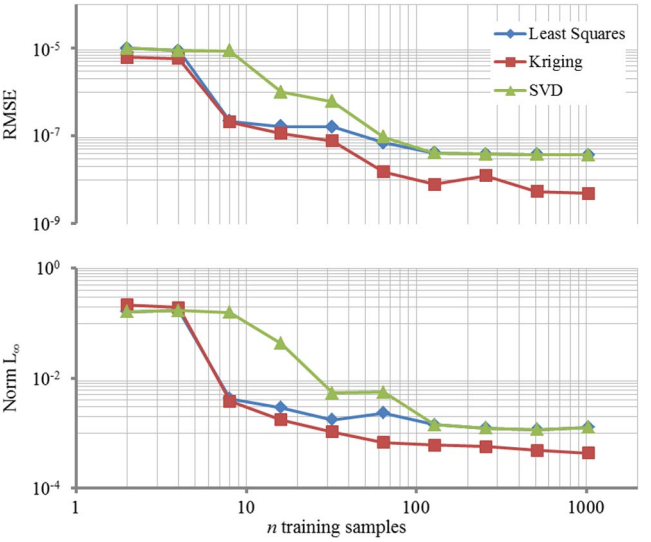

Fig. 12 Effect of training sample size on the accuracy of ROMs generated from three different approaches.

RSME continued to reduce as additional training samples were added until $n = 1024$, with the exception of the zeroth-order regression and general exponential (expg) formulation, which appeared to be especially sensitive to the pseudorandom LHS sampling pattern. This is evident by the uneven and erratic shape of the maximum RMSE line in Fig. 11. Kriging was found to be the most accurate ROM type of those considered. For all ROM types, a steady decline in the normalized L_∞ was observed, and all ROM types showed approximately the same order of normalized L_∞ for $n > 100$. Some minor noise was observed due to the random nature of the LHS method, but the overall trend that more training samples resulted in lower measures of error was clear. For the largest training set size considered, the least-squares cubic model, 25 bases SVD model with

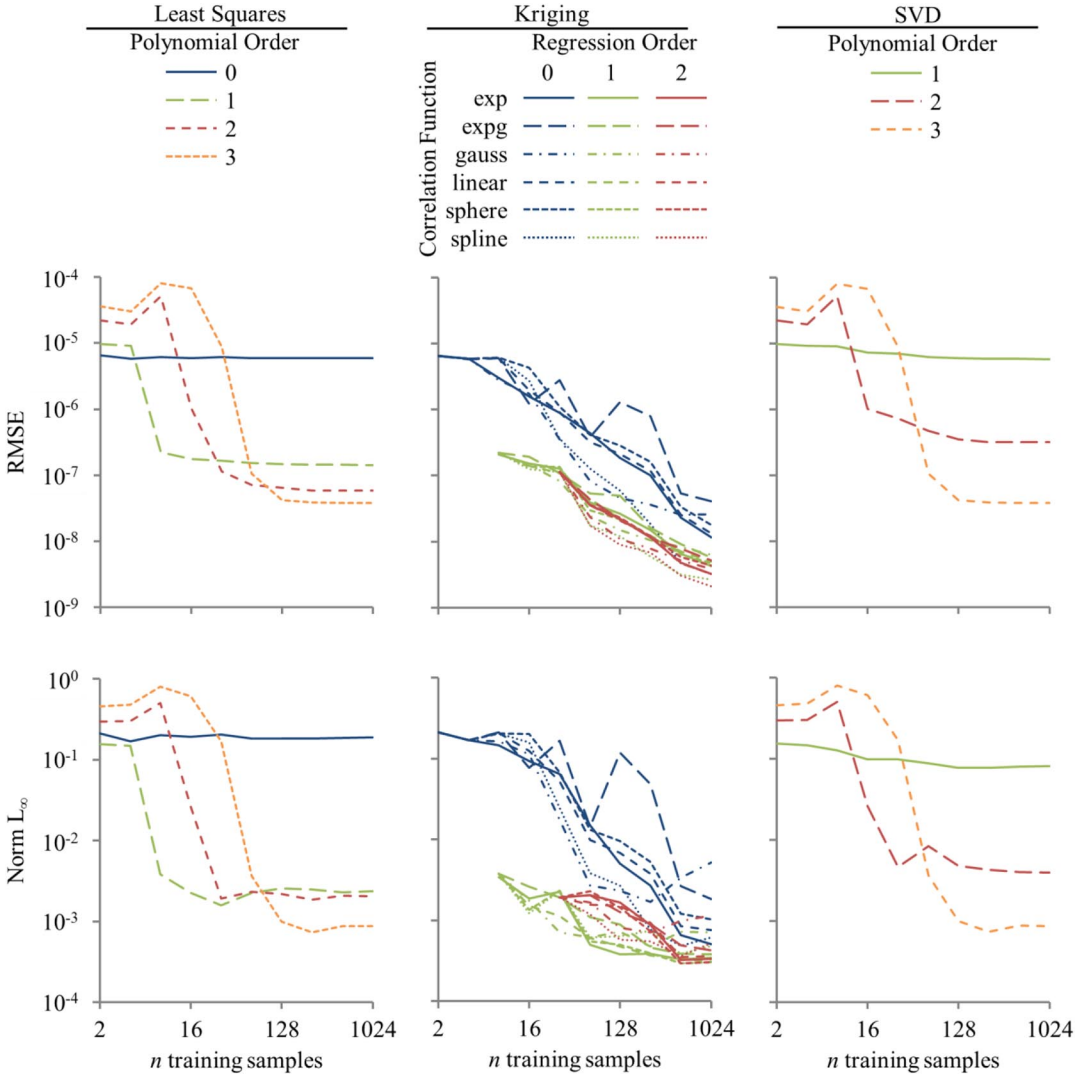

Fig. 11 Error of each ROM type for a given training set sample size.

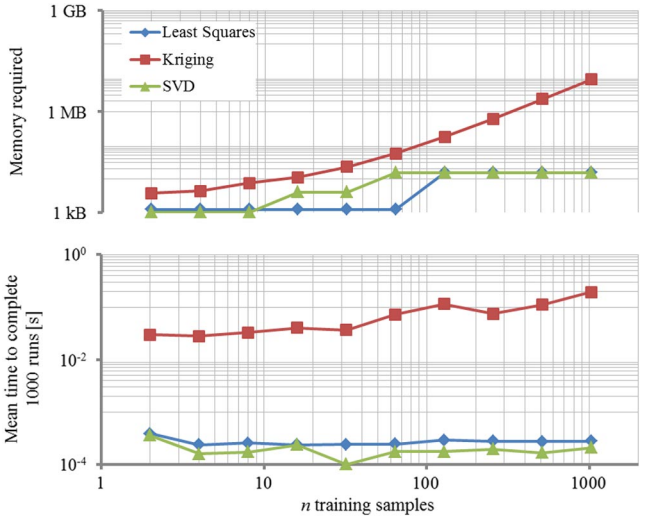

Fig. 13 Effect of training sample size on the computational cost of ROMs generated from three different approaches.

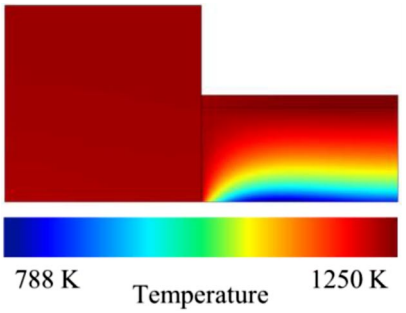

Fig. 14 Mean temperature distribution.

cubic regression, and kriging model with a quadratic regression and spherical correlation were found to be the most accurate of their respective ROM types.

D. Reduced-Order Model Computational Efficiency

Also critical to evaluation of a ROM's utility is the computational efficiency of a ROM. To quantify computational efficiency, the amount of computer memory the ROM must occupy and the time required for the ROM to be executed were considered. For each of the ROM types and training sets, the memory consumption and execution time required to run the $k = 1000$ test samples were recorded and are shown in Fig. 13. It can be seen that, although the kriging ROM was the most accurate, this accuracy came at the price of rapidly growing memory requirements and slower execution times than the least-squares and SVD ROMs. This agreed with intuition because the method of kriging is able to reproduce the entire training set and thus contains all of the information used to train the ROM. The least-squares and SVD approaches did not have the ability to reproduce the training set and thus retained only a fraction of the information used to train the ROMs, which resulted in lower memory requirements for the computer.

In terms of processing speed, the least-squares and SVD ROMs were roughly two orders of magnitude faster than kriging. The SVD ROM was also slightly faster than the least-squares ROM; however, at these submillisecond scales, the specific implementation of the models and state of the computer's background programs may influence which of these two ROMs would be processed more quickly. To reduce random fluctuations in processing speed, each ROM was run 10 times, timed using the tic and toc functions of Matlab, and the results averaged.

E. Comparison to Finite Element Analysis

As a check of ROM accuracy and efficiency, simulations of the generalized thermal problem with constant thermal properties and with each ROM approach were conducted. The sample structure was

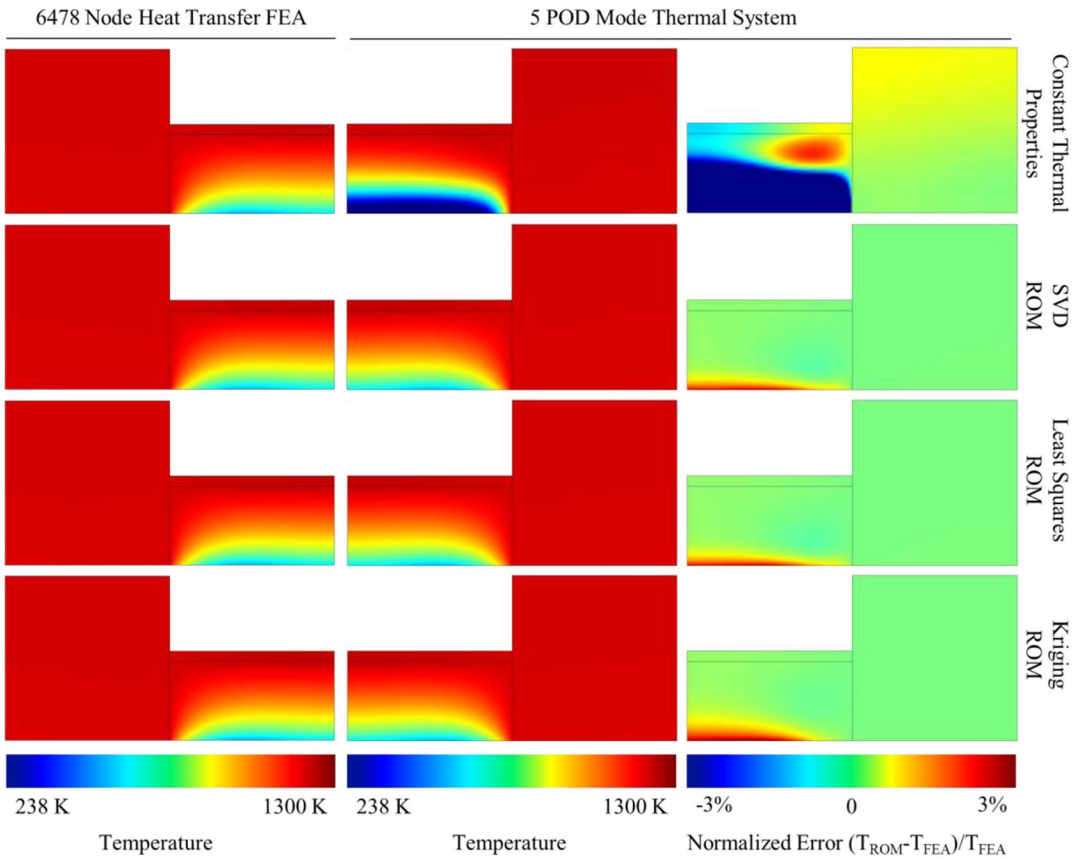

Fig. 15 Significant qualitative improvement when using the thermal property ROMs with the five-mode thermal system compared to with constant thermal properties.

Table 1 Simulation performance of each ROM approach

Thermal property ROM	Processing time, s	RMSE, K
None	2.6	167.7
SVD	6.3	2.2
Least-squares	6.3	2.2
Kriging	62.5	2.8

started at a uniform 1260 K, similar to the structure temperature at the initiation of the terminal phase of the trajectory. A steady outward heat flux was then applied with the spatial distribution

$$\dot{q}_w = -20341.7[\exp(-100x + 4)/10 + 0.9] \tag{14}$$

to simulate a cooling boundary layer with a logarithmic thickness profile. Here, x is the distance in meters from the ballast edge farthest from the TPS, and $\dot{q}_w$ is the heat flux in watts per square meter. This is not physical because the boundary layer imposing the heat flux would change with the change in the wall boundary conditions. However, the accuracy of the boundary layer heat flux is not the focus of this paper, and a consistent heat flux profile allowed for direct comparison of the methods. The constant thermal properties were taken from the materials at the mean temperature distribution observed during the FEA simulation shown in Fig. 14.

All thermal problems were integrated for 37.5 s, the duration of the terminal phase of the trajectory. The final temperature distributions for the FEA, five-POD-mode generalized system with constant thermal properties, and five-POD-mode generalized system with the SVD, least-squares fit, and kriging ROMs varying the thermal properties can be seen in Fig. 15. An overall improvement in the agreement between the FEA and five-POD-mode system solutions is evident when using the ROMs to model the thermal properties of the substructure. Processing times and final error measurements for each approach are shown in Table 1. As expected, kriging was the slowest, increasing the total processing time for the simulation by a factor of 24. SVD and least-squares were much faster and slowed the simulation by a factor of 2.4. The SVD and least-squares approaches provided the lowest final RMSE of the temperature field. However, all of the approaches vastly improved the accuracy of the simulation compared to using no thermal property model. It is likely that the RMSE of about 2 K arose from generalization of the governing equations with the five thermal modes rather than the thermal property ROMs.

F. Variation of Singular Value Decomposition Reduced-Order Model Number of Thermal Modes

Because the SVD ROM approach is novel to this type of problem, the effect of varying the number of retained thermal modes was also studied. Using the methods previously described, SVD ROMs that considered the top two, five, and eight POD thermal modes were trained and used to simulate the steady-heat-flux case in the previous section. The temperature range of each simulation compared to the FEA solution is shown in Fig. 16 and RMSE in Fig. 17. It can be seen that using only two modes provided a reasonable range of temperatures for much of the simulation but was unable to accurately express the initial temperature profile. Further modes first refined the initial portion of the solution when five modes were included and later refined the later portion when eight modes are included. A final RMSE as low as 0.4 K is shown in Fig. 17 when eight modes are included.

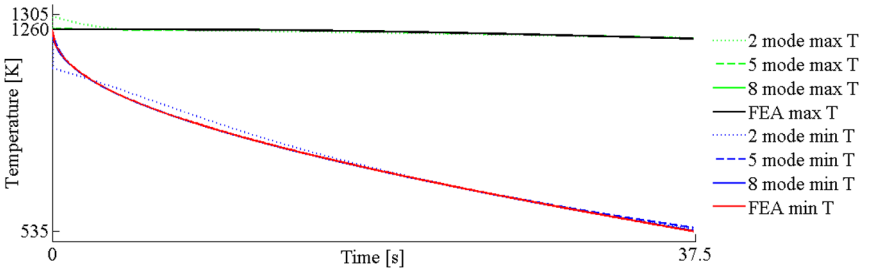

Fig. 16 Temperature range of SVD ROM simulation converges on FEA solution as the number of retained thermal modes is increased.

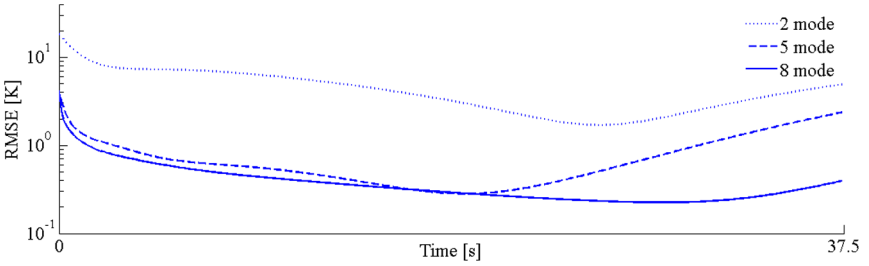

Fig. 17 Convergence of SVD ROM to FEA solution with increasing number of retained thermal modes.

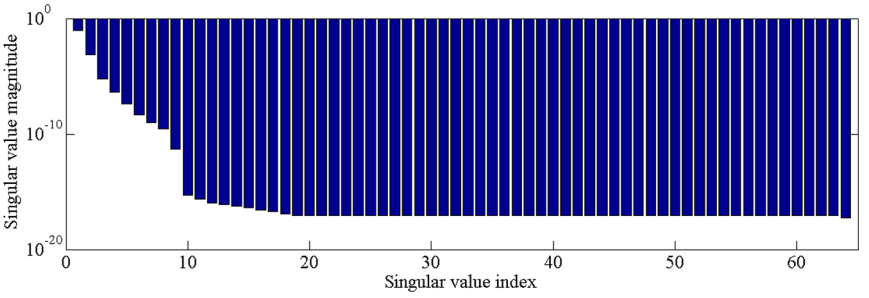

Fig. 18 Sorted singular values of the eight thermal mode snapshot matrix.

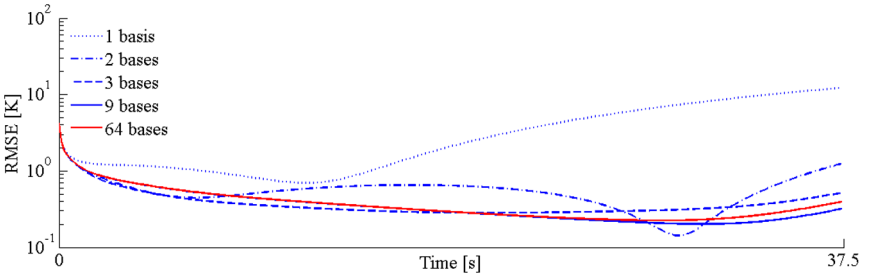

Fig. 19 Low RMSE compared to FEA when as few as three SVD bases are retained.

G. Truncation of Singular Value Decomposition Bases

In some cases, it may be impractical to perform a full SVD on the snapshot matrix. This could be due to the matrix being too large because it contains too many degrees of freedom, snapshots, or both. In such a scenario, the Lanczos algorithm or some other method may be used to find only most important singular values and bases. A threshold value could be chosen by the engineer, below which the singular values and bases would be neglected. This truncation of the SVD bases may degrade the accuracy of the final ROM, but as long as the most dominant bases are retained, this degradation would be minimal. Figure 18 shows the sorted magnitudes of the singular values of the eight-thermal-mode snapshot matrix. It can be determined from the singular values that bases 1 through 9 dominate the solution space, whereas higher bases are negligible. Therefore, neglecting these higher bases still produced a good SVD ROM. From Fig. 19, it can be seen that this was the case because SVD ROMs generated with truncated bases continue to closely match the temperature ranges of the FEA solution during simulation and have very small errors compared to retaining the full, 64-base set.

V. Conclusions

Three reduced-order models were applied to the problem of modeling the thermal conductivity and capacity variation with respect to temperature for a sample substructure of a hypersonic vehicle. The thermal problem was first reduced through projection of the thermal states into bases determined by proper orthogonal decomposition. A relative error of order 10^{-8} was determined when the POD bases were truncated to the top five most prominent thermal modes. A Latin hypercube sample distribution of the thermal mode coordinates was then used to determine a sample set of generalized thermal conductivity and capacity matrices for the substructure. Various numbers of these samples were then used to create least-squares fit polynomial, kriging, and singular-value decomposition based ROMs. These ROMs were then compared in terms of error compared to FEA solutions and numerical efficiency.

The SVD ROM was determined to be the superior approach. For relatively small training sample sizes of around 200, this ROM provided similar accuracy to the least-squares and kriging methods. However, the SVD ROM also required up to approximately 600 times less memory than the kriging ROM and was similar to the least-squares ROM. The SVD ROM was also capable of execution slightly faster than the least-squares ROM and roughly 100 times faster than the kriging ROM.

Integration of the five-mode generalized thermal problem was then performed with constant thermal properties and thermal properties varied according to the SVD, least-squares, and kriging ROMs. Generalized solutions were compared to a full-order FEA solution with empirical thermal properties. Significant qualitative improvements were evident, lending to the importance and utility of a thermal conductivity and capacity ROM for thermal problems spanning wide temperature ranges.

Finally, the effect of the number of retained thermal modes and number of retained SVD bases on the performance of the SVD ROM during simulation was considered. Including more thermal modes improved the quality of the ROM solution, as expected. However, as few as three SVD bases provided excellent agreement with the FEA solution with an RMSE between 0.5 and 4.2 K.

Acknowledgments

This work was sponsored by the U.S. Air Force Research Laboratory, Munitions Directorate, Eglin Air Force Base, Florida. The technical monitors are Crystal Pasiliao and Daniel Reasor. Opinions, interpretations, conclusions, and recommendations are those of the authors and are not necessarily endorsed by the U.S. Government.

References

[1] Falkiewicz, N. J., and Cesnik, C. E. S., "Proper Orthogonal Decomposition for Reduced-Order Thermal Solution in Hypersonic Aerothermoelastic Simulations," *AIAA Journal*, Vol. 49, No. 5, 2011, pp. 994–1009. doi:10.2514/1.J050701

[2] Falkiewicz, N. J., and Cesnik, C. E. S., "Enhanced Modal Solutions for Structural Dynamics in Aerothermoelastic Analysis," *52nd AIAA/ASME/ASCE/AHS/ASC Structures, Structural Dynamics and Materials Conference*, AIAA Paper 2011-1963, April 2011.

[3] Bialecki, R. A., Kassab, A. J., and Fic, A., "Reduction of the Dimensionality of Transient FEM Solutions Using Proper Orthogonal Decomposition," *36th AIAA Thermophysics Conference*, AIAA Paper 2003-4207, June 2003.

[4] Qian, J., Wang, Y., Song, H., Pant, K., Peabody, H., Ku, J., and Butler, C. D., "Projection-Based Reduced-Order Modeling for Spacecraft Thermal Analysis," *Journal of Spacecraft and Rockets*, Vol. 52, No. 3, June 2015, pp. 978–989. doi:10.2514/1.A33117

[5] Liang, Y. C., Lee, H. P., Lim, S. P., Lin, W. Z., Lee, K. H., and Wu, C. G., "Proper Orthogonal Decomposition and its Applications—Part 1: Theory," *Journal of Sound and Vibration*, Vol. 252, No. 3, 2002, pp. 527–544. doi:10.1006/jsvi.2001.4041

[6] Bialecki, R. A., Kassab, A. J., and Fic, A., "Proper Orthogonal Decomposition and Modal Analysis for Acceleration of Transient FEM Thermal Analysis," *International Journal for Numerical Methods in Engineering*, Vol. 62, No. 6, 2005, pp. 774–797. doi:10.1002/(ISSN)1097-0207

[7] McMasters, R. L., Zhou, Z., Dowding, K. J., Somerton, C., and Beck, J. V., "Exact Solution for Nonlinear Thermal Diffusion and Its Use for Verification," *Journal of Thermodynamics and Heat Transfer*, Vol. 16, No. 3, 2002, pp. 366–372.

[8] Matney, A. K., Mignolet, M. P., Spottswood, S. M., Culler, A. J., and McNamara, J. J., "Thermal Reduced Order Model Adaptation to Aero-Thermo-Structural Interactions," *55th AIAA/ASME/ASCE/AHS/ASC Structures, Structural Dynamics, and Materials Conference*, AIAA Paper 2014-0493, Jan. 2014.

[9] Ashley, H., and Zartarian, G., "Piston Theory—A New Aerodynamic Tool for the Aeroelastician," *Journal of the Aeronautical Sciences*, Vol. 23, No. 12, 1956, pp. 1109–1118. doi:10.2514/8.3740

[10] Eckert, E. R. G., "Use of Reference Enthalpy in Specifying the Laminar Heat-Transfer Distribution Around Blunt Bodies in Dissociated Air," *Journal of Aerospace Sciences*, Vol. 27, No. 6, 1960, pp. 464–466. doi:10.2514/8.8587

[11] Camarda, C. J., Haftka, R. T., and Riley, M. F., "An Evaluation of Higher-Order Modal Methods for Calculating Transient Structural Response," *Journal of Computer and Structures*, Vol. 27, No. 1, 1987, pp. 89–101. doi:10.1016/0045-7949(87)90184-2

[12] Camarda, C. J., "Development of Advanced Modal Methods for Calculating Transient Thermal and Structural Response," NASA TM 104102, 1991.

[13] Balakrishnan, N., Hou, G., and Camarda, C., "Nonlinear Transient Thermal Analysis by the Force-Derivative Method," *40th Structures, Structural Dynamics, and Materials Conference and Exhibit*, AIAA Paper 1999-1398, 1999.

[14] Pasiliao, C. L., Sytsma, M. J., Neergaard, L. J., Witeof, Z. D., and Trolier, J. W., "Preliminary Aerothermal Structural Simulation," *14th AIAA Aviation Technology, Integration, and Operation Conference*, AIAA Paper 2014-2292, 2014.

[15] Witeof, Z. D., and Neergaard, L. J., "Initial Concept 3.0 Finite Element Model Definition," U.S. Air Force Research Lab. Rept. AFRL-RWWV-TN-2014-0013, Eglin AFB, FL, April 2014.

[16] Trolier, J. W., Hall, D. W., Hudson, D. J., and Torres, M., "Aerothermal Targets Analysis Program (ATAP): Volume 2—Engineering Document," Science Applications International Corporation (SAIC) Rept. 95/1022, Tysons Center, VA, 2004.

[17] Golub, G. H., and Kahan, W., "Calculating the Singular Values and Pseudo-Inverse of a Matrix," *Journal of the Society for Industrial and Applied Mathematics: Series B, Numerical Analyses*, Vol. 2, No. 2, 1965, pp. 205–224.

[18] Hughes, T. J. R., "Unconditionally Stable Algorithms for Nonlinear Heat Conduction," *Computer Methods in Applied Mechanics and Engineering*, Vol. 10, No. 2, 1977, pp. 135–139. doi:10.1016/0045-7825(77)90001-9

[19] Sacks, J., Welch, W. J., Mitchell, T. J., and Wynn, H. P., "Design and Analysis of Computer Experiments," *Statistical Science*, Vol. 4, No. 4, 1989, pp. 409–435.

[20] Martin, J. D., "Robust Kriging Models," *51st AIAA/ASME/ASCE/AHS/ASC Structures, Structural Dynamics, and Materials Conference*, AIAA Paper 2010-2854, April 2010.

[21] McKay, M., Beckman, R., and Conover, W., " Comparison of Three Methods for Selecting Values of Input Variables in the Analysis of Output from a Computer Code," *Technometrics, American Statistical Association*, Vol. 21, No. 2, May 1979, pp. 239–245.

[22] Manteufel, R. D., "Evaluating the Convergence of Latin Hypercube Sampling," *41st AIAA/ASME/ASCE/AHS/ASC Structures, Structural Dynamics, and Materials Conference and Exhibit*, AIAA Paper 2000-1636, April 2000.

[23] Lophaven, S. N., Nielsen, H. B., and Søndergaard, J., "DACE—A Matlab Kriging Toolbox," Informatics and Mathematical Modeling, Technical Univ. of Denmark Technical Rept. IMM-TR-2002-12, Kongens Lyngby, Denmark, 2002.

[24] Lillian, C. S., McDaniel, D. R., and Morton, S. A., "An Efficient Method of Computing Maneuvering Aircraft Surface Loads Using CFD, Proper Orthogonal Decomposition, and System Identification," *49th AIAA Aerospace Sciences Meeting*, AIAA Paper 2011-1177, Jan. 2011.

[25] Klock, R. J., and Cesnik, C. E. S., "Aerothermoelastic Reduced Order Model of a Hypersonic Vehicle," *AIAA Atmospheric Flight Mechanics Conference*, AIAA Paper 2015-2711, June 2015.

[26] "Acusil II Thermal Protection System," Exelis, Colorado Springs, CO, Jan. 2013, https://d2cy52pj4xpl74.cloudfront.net/file/502ca1c8-267c-48e8-a770-e085a4083154/503a237a-5fb3-4a2a-8ac5-5d6f50576be8/503a237a-5fb3-4a2a-8ac5-5d6f50576be8.pdf?version=1 [retrieved 6 March 2017].

[27] Ohlhorst, C. W., Vaughn, W. L., Ransone, P. O., and Tsou, H., "Thermal Conductivity Database of Various Structural Carbon-Carbon Composite Materials," NASA TM 4787, 1997.

[28] Rehmer, B., Beckmann, J., Finn, M., and Glaubitz, S., "Determination of Elastic Moduli of C/C-Composite at Temperatures up to 1900C," Federal Inst. for Materials Research and Testing Rept. 2004-157bg, Berlin, 2004.

[29] Fitzer, E., and Manocha, L. M., *Carbon Reinforcements and Carbon/Carbon Composites*, Springer–Verlag, Berlin, 1998, pp. 254–256.

[30] "Young Modulus of Elasticity for Metals and Alloys," The Engineering Toolbox, Jan. 1995, http://www.engineeringtoolbox.com/young-modulus-d_773.html [retrieved April 2015].

[31] "Metals—Specific Heats," The Engineering Toolbox, http://www.engineeringtoolbox.com/specific-heat-metals-d_152.html [retrieved April 2015].

[32] "ATI Ti-6Al-4V, Grade 5, Technical Data Sheet," Allegheny Technologies Incorporated, Pittsburg, PA, Jan. 2012, https://www.atimetals.com/Products/Documents/datasheets/titanium/alloyed/ati_6-4_tds_en_v1.pdf [retrieved 6 March 2017].

[33] Schmidt, F. F., and Ogden, H. R., "The Engineering Properties of Tungsten and Tungsten Alloys," Defense Metals Information Center AD 425547, Columbus, OH, 1963.

[34] Abaqus FEM/CAE, Software Package, Ver. 6.12, Dassault Systemes Simulia Corp., Providence, RI, 2012.

T. L. Jackson
Associate Editor